



Article

Block Copolymer-Assisted Synthesis of Iron Oxide Nanoparticles for Effective Removal of Congo Red

Mohan K. Bhattarai ^{1,*}, Moses D. Ashie ², Sita Dugu ¹, Kiran Subedi ³, Bishnu P. Bastakoti ^{2,*}, Gerardo Morell ¹ and Ram S. Katiyar ¹

- Department of Physics, University of Puerto Rico, P.O. Box 70377, San Juan, PR 00936-8377, USA
- Department of Chemistry, North Carolina A&T State University, 1601 East Market Street, Greensboro, NC 27411, USA
- ³ Analytical Services Laboratory, College of Agriculture and Environmental Sciences, North Carolina A&T State University, 1601 East Market Street, Greensboro, NC 27411, USA
- * Correspondence: mohankbhattarai@gmail.com (M.K.B.); bpbastakoti@ncat.edu (B.P.B.)

Abstract: Iron oxide nanoparticles (IONPs) were synthesized via a block copolymer-assisted hydrothermal method and the phase purity and the crystal structure were investigated by X-ray diffraction. The Rietveld analysis of X-ray diffractometer spectra shows the hexagonal phase symmetry of α -Fe₂O₃. Further, the vibrational study suggests Raman active modes: 2A1g + 5Eg associated with α -Fe₂O₃, which corroborates the Rietveld analysis and orbital analysis of 2PFe. The superparamagnetic behavior is confirmed by magnetic measurements performed by the physical properties measurement system. The systematic study of the Congo red (CR) interaction with IONPs using a UV-visible spectrophotometer and a liquid chromatography–tandem mass spectrometry system equipped with a triple quadrupole mass analyzer and an electrospray ionization interface shows effective adsorption. In visible light, the Fe₂O₃ nanoparticles get easily excited and generate electrons and holes. The photogenerated electrons reduce the Fe³⁺ ions to Fe²⁺ ions. The Fe²⁺/H₂O₂ oxidizes CR by the Fenton mechanism. The strong adsorption ability of prepared nanoparticles towards dyes attributes the potential candidates for wastewater treatment and other catalytic applications.

Keywords: Rietveld; vibrational study; IONPs; block copolymer; hydrothermal; adsorption; α -Fe₂O₃; superparamagnetism



Citation: Bhattarai, M.K.; Ashie, M.D.; Dugu, S.; Subedi, K.; Bastakoti, B.P.; Morell, G.; Katiyar, R.S. Block Copolymer-Assisted Synthesis of Iron Oxide Nanoparticles for Effective Removal of Congo Red. *Molecules* 2023, 28, 1914. https://doi.org/10.3390/molecules28041914

Academic Editor: Liang Huang

Received: 26 January 2023 Revised: 12 February 2023 Accepted: 15 February 2023 Published: 17 February 2023



Copyright: © 2023 by the authors. Licensee MDPI, Basel, Switzerland. This article is an open access article distributed under the terms and conditions of the Creative Commons Attribution (CC BY) license (https://creativecommons.org/licenses/by/4.0/).

1. Introduction

Metal oxide nanoparticles show size-dependent physical, chemical, electronic, and magnetic properties that constitute versatile platforms for producing materials with possible applications in catalysis and magnetic and optical devices [1–3]. The studies have shown that the catalytic and magnetic properties of nanoparticles can be quite different from other bulk materials. When the size of the nanoparticles is below a critical value, or depending on the material, nanoparticles (NPs) behave like a giant paramagnetic atom with a single magnetic domain, exhibiting superparamagnetic behavior [2]. Fe₂O₃ nanoparticles show superparamagnetic with a size-dependent blocking temperature [4] and enhanced catalytic properties compared to bulk materials [5]. Since the surface-to-volume ratio increases with decreasing nanoparticle diameters, surface effects contribute to those properties. However, there are some challenges in tuning the magnetization, stability, capture efficiency, and surface properties of iron oxide nanoparticles (IONPs) [2]. The nanomaterials with a high surface area are important in established processes such as catalysis and molecular separations alongside emerging technologies for energy and health [6,7]. Multiple components, such as the size of the iron oxide crystals, the charge, the nature of the coating, and the hydrodynamic size of the coated particle, have to be measured accurately, as far as possible, for their effective application [8].

Molecules **2023**, 28, 1914 2 of 13

Improvements to metal oxide nanoparticle characteristics, such as enhanced magnetic properties, non-biofouling surface coatings, and the integration of multifunctional ligands, continue improving its potential applications. Superparamagnetic iron oxide nanoparticles (SPIONs) are among the most used nanoparticle in biomedical fields as contrast agents for magnetic resonance imaging, drug delivery systems, or hyperthermia agents in cancer therapies [9]. The superparamagnetic and high surface area of Fe_2O_3 nanomaterials can remove heavy metal arsenic ions in water, promising materials for wastewater treatment [10] and different types of coupling reactions [6]. The magnetic properties of iron oxide nanoparticles make them easily recyclable and can be used multiple times. This facilitates the application and cost management in the use of magnetic nanoparticles, while at the same time, minimizing the number of times materials have to be synthesized. The Fe_2O_3 nanoparticles were successfully used for the catalytic destruction of ethane, where the presence of oxygen vacancies and lattice defects enables the oxygen transfer speed and redox capabilities of Fe_2O_3 [11].

Water purification has recently gained significant attention as it is contaminated due to different anthropogenic activities. Pesticides from agricultural activities, fecal-related contaminants releasing pathogens, domestic wastes, and industrial effluents are a few sources of water pollutants. Among the chemical pollutants, organic dyes, due to their toxic nature, are one of the major contaminants of industrial water. Therefore, continuous efforts are ongoing to effectively deal with industrial wastewater containing organic pollutants. Congo red (CR) is widely used to dye fabrics and stain tissues. Despite its usefulness, releasing large quantities of CR can be harmful and cause environmental pollution. Carcinogenicity and various toxicities associated with CR that affect flora, fauna, and humans mean there is an urgency for removing CR from wastewater.

Nanotechnology has been an exceptional development for water treatment compared to costly conventional treatment methods and remediation from microorganisms and organic dyes [12]. Catalytic adsorption of dyes is, therefore, of great interest as the molecules of the dyes are removed for safe industrial handling of excess pollutants and safe disposal of effluents. The need for remediation of wastewater challenges has caused the development of different heterogeneous inorganic catalysts/adsorbents, which find application in adsorption and degradation [13,14]. IONPs are abundant, easily accessible, environmentally compatible, and have high stability, low cost, and suitable magnetic properties. Various methods have been developed to prepare IONPs [15–18], although they are prone to aggregate during synthesis, which limits their applications. Many physical and chemical approaches are used to avoid this limitation. Numerous synthetic routes have been developed to produce magnetic nanoparticles with good control of shape, size, and distribution. Iron oxide, in most cases, can be synthesized either by top-down or bottom-up techniques. Lots of different mechanical and physical techniques, such as ultrasonication, irradiation, laser ablation, microwave, and electrochemical, and physical vapor deposition, are used in top-down approaches to produce magnetic nanoparticles by using green methods [19]. In particular, these environmentally friendly methods transform the bulk phase material into nanometer sizes. Top-down options are preferred in the industry because they are more straightforward, less expensive, and easy to scale up production with. Although it is a viable green technique and requires limited manual operation, particle functionalization will be more problematic, and the resulting nanoparticles, through these inexpensive routes, will be in a wide distribution of size and shapes, which directly limits their utilization for biological applications [9,20]. A wide range of nanoparticles have been synthesized by mechanochemical processing, which is an alternative technique to synthesize particles with a mean size as low as 4 nm, low agglomeration, narrow size distributions, and uniformity of crystal structure and morphology [21].

Conversely, bottom-up techniques (also known as wet chemistry routes) refer to the chemical synthesis of nanoparticles, wherein the primary nucleation of nanomaterials followed by growth and aggregation will finally result in desired nanoparticles with specific sizes and shapes [22]. Various materials, such as proteins, polysaccharides, and synthetic

Molecules **2023**, 28, 1914 3 of 13

polymers, are used to prepare nanoparticles. The choice of matrix materials depends upon many factors including the required size of nanoparticles, surface characteristics, degree of biocompatibility, degree of biodegradability, and toxicity [2]. Moreno et.al reported the addition of acids in the sol-gel preparation of γ -Fe₂O₃/SiO₂ to obtain single-phase γ -Fe₂O₃ magnetic nanoparticles with controllable particle size and size, while the distribution opens a new method for the design of nanocomposites for different applications [23]. The natural zeolite-type clinoptilolite NPs were synthesized by using the chemical solution method to investigate their degradation ability subjected to methyl orange [24]. Tsang et al. synthesized iron-based magnetic nanometer-sized particles (FeNi, Fe₃C) using a wet chemical method (sequential spraying followed by chemical precipitation, and controlled pyrolysis), which is a promising nanocomposite catalyst for the production of fine chemicals in liquid-phase reactions [25]. Such types of magnetic nanoparticles are also crucial in several areas of the nanotechnology field. The simple thermal decomposition method was carried out to synthesize truncated cubic iron oxide nanoparticles [26] promising SPIONs for MRI contrast agents. Spherical dots of SPIONs, the size ranging from 7.8 to 17.9 nm, were synthesized via thermal decomposition methods [27]. Macromolecules, including block copolymers, surfactants, and ionic liquids are widely used as a template and structure-directing agent to synthesize magnetic nanoparticles [16,28]. Specially designed block copolymers are a boon for the controlled synthesis of nanoparticles. The hydrophilic section of the amphiphilic block copolymers interacts with inorganic precursors, and the hydrophobic block works as a template to synthesize the porous nanoparticles [29,30]. Highly biocompatible porous Fe₂O₃ microspheres have been synthesized with a double hydrophilic block copolymer, polyethylene-block-polyacrylic acid (PEO-b-PAA) with a high loading capacity of drug molecules, which could be promising nanoparticles for magnetically guided nanocarriers [31]. The hydrophilic and anionic PAA block strongly interacts with ferric ions. Nucleation of the Fe₂O₃ nanoparticles is expected in the presence of a precipitating agent in an aqueous solution. At the same time, the neutral PEO corona stabilizes the primary nanoparticles, which ultimately undergo self-assembly to form the microspheres of Fe₂O₃ at elevated temperatures. The various promising features of polymers have been reported, thus, can enhance the physical and chemical properties of materials for subsequent suitable potential applications [32].

In this study, the bottom-up approach was used to fabricate IONPs. The main advantages of this approach are producing a nanostructure with fewer defects, a more homogeneous chemical composition, a control reaction mechanism, size, and optimization. There are many reports on the synthesis and applications of iron oxides for wastewater treatment. However, the current work uses amphiphilic block copolymers to synthesize sub-50 nm iron oxide nanoparticles with pores. Unlike in the previous work, the F127 block copolymer plays a dual role as a structure-directing agent and a porogen. The pore size on the nanoparticles is almost similar to the size of polymeric micelles. The IONPs were characterized using different techniques, including Fourier transform infrared (FTIR) spectroscopy, scanning electron microscopy (SEM), transmission electron microscopy (TEM), Raman spectroscopy, x-ray photoelectron spectroscopy (XPS), x-ray diffraction (XRD) and cryogen-free physical property measurement system (PPMS). The nanoparticles possess an abundance of sites and surface area for reactions. The Rietveld analysis of x-ray diffractometer spectra shows the hexagonal phase symmetry of α -Fe₂O₃ nanoparticles. A thorough study was performed to explore whether the dyes degrade or adsorb the nanoparticles. The systematic study was performed on the adsorption of model dyes, Congo red (CR), using an UV visible spectrophotometer and LC-MS/MS triple quadrupole with an electrospray ionization mass spectrometer. It shows that a significant number of dyes adsorbed by the nanoparticles get degraded in the presence of the oxidizing agent, H₂O₂, one of the components of the Fenton reaction.

Molecules **2023**, 28, 1914 4 of 13

2. Results and Discussion

In nanoparticle synthesis, the surfactant undergoes self-assembled molecular clusters in a solution and is adsorbed by the interface between a solution and a different phase (solution/solids) [33]. We chose F127 as a template because of its availability, cheaper price, and known chemistry. It helps to control the size of the NPs, excels the adsorption efficiency, and enhances the superparamagnetic properties of magnetic nanoparticles [27,34]. The slow hydrolysis of urea releases ammonia, forming a complex with metal ions. The coordinated NH₃ molecules interact with the polyethylene oxide chains (PEO) of the F127 units through hydrogen bonding, which is a driving force for the interaction of metal ions with the polymer [35]. Figure 1a shows the SEM images of IONPs. The particle size distribution graph of nanoparticles proves that F127 works as an effective structure-directing agent (Figure S1). The micelles of F127 wrap around the nanoparticles and prevent crystal growth. The aggregation of NPs is unavoidable in the absence of a polymer (Figure S2). TEM imaging was performed to explore the internal structure of nanoparticles. Multiple pores around 10 nm were in the TEM image (Figure 1b) showing the porogenic ability of F127. The TEM image shows a characteristic particle diameter of approximately 50 nm. As the concentration of the polymer in the solution is above the critical micelles concentration, then, colloidal nano aggregates (micelles) are formed. The inorganic precursors deposit around the micelles and the calcination remove the organic moieties leaving porosity on the inorganic nanostructure. The space occupied by micelles leads to the pores. The pore size is matched with the diameter of micelles of F127 in an aqueous solution [36]. The hydrodynamic diameter was found to be 310 nm with a polydispersity index of 0.3. The size is larger than the size obtained from electron microscopy. It is probably due to the aggregation of inorganic nanoparticles. Additionally, DLS measurements were carried out in solution, and the TEM measurements were made on a dry sample under a high vacuum. The nanoparticles have a -21 mV surface charge at pH 6.6. The removal of the polymer was monitored by FTIR spectra. The signature peaks of the polymer disappeared after calcination (Figure 2a). The characteristic peaks of FTIR at 573 cm⁻¹, 787 cm⁻¹, and 882 cm⁻¹ are attributed to the Fe-O bond of Fe₂O₃. The EDX spectrum, shown in Figure 2b, confirms the presence of the O and Fe elements along with their respective characteristic X-ray emission lines (O: $K\alpha$ 0.5249 keV, Fe: $L\alpha$ 0.7048 keV, Fe: $K\alpha$ 6.4006 keV, Fe: $K\beta$ 7.0563 keV). Then, we carried out XPS measurements to further confirm the elemental composition and analyze the orbital state of the Fe element. Casa XPS v2.3 software was used to fit the XPS spectra. In this study, the binding energy of the Fe $2p_{3/2}$ and Fe $2p_{1/2}$ are obtained at 710.67 eV and 723.89 eV, respectively, (Figure 2c), which are similar to previous reports [37–39]. The Fe $2p_{3/2}$ and Fe $2p_{1/2}$ are further deconvoluted into Fe²⁺ and Fe³⁺ ions. The major peak at 710.67 eV confirms that the characteristic peak from Fe $2p_{3/2}$ core level electrons is attributed to Fe³⁺ [40] and the peak at 723.89 eV confirms that Fe²⁺ is in the octahedral sites. The Fe²⁺ ions are fundamental to determining the magnetic moment in the lattice [40,41]. The satellite peak associated with Fe $2p_{3/2}$, which appeared at approximately 719 eV, is evidence of the Fe³⁺ ions [38,40] supporting the Fe₂O₃ form of the IONPs. Corroborating these results with XRD and Raman analysis, confirmed that the prepared IONPs are dominant features of α -Fe₂O₃.

Molecules **2023**, 28, 1914 5 of 13

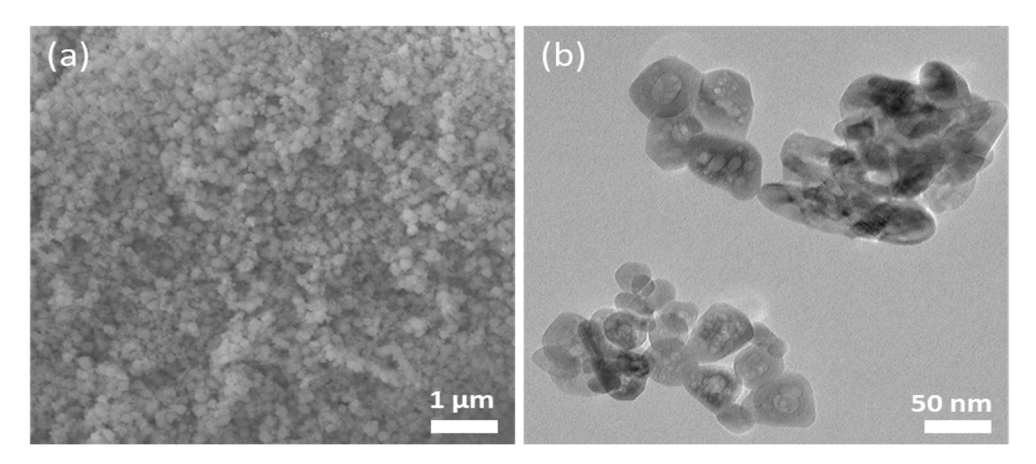


Figure 1. (a) SEM and (b) TEM images of the IONPs.

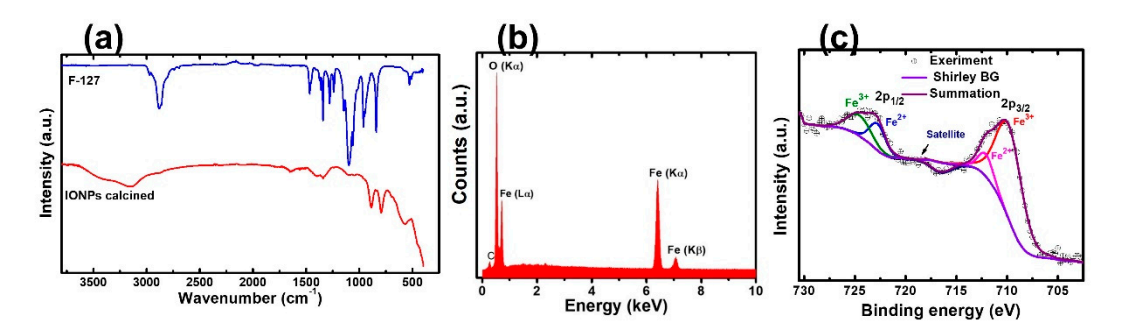


Figure 2. (a) FTIR spectra of polymer and IONPs. (b) EDX spectrum of IONPs. (c) XPS graph of Fe atoms showing the deconvolution at $2p_{1/2}$ and $2p_{3/2}$.

The XRD patterns with the Rietveld analysis (Figure 3a) indicate that the IONPs are polycrystalline and exhibit well-defined diffraction peaks matched with the JCPDS # 330664, which suggests a hexagonal (R3C) crystal structure. Various investigations have suggested hexagonal phase symmetry for the IONPs [42,43]. The crystallographic database file COD: 9016457 (R3C) CIF [44] was used for the reference phase of the sample, and the pseudo-Voigt function was used for the profile simulation in the FullProf suite software [45]. The Rietveld refinement analysis supported the hexagonal (R3C) phase symmetry of a sample, as reported for α -Fe₂O₃ [46,47]. The inset figure shows the crystal structure visualization of IONPs, showing red-colored O atoms and green-colored Fe atoms. However, both forms of the α -Fe₂O₃ and γ -Fe₂O₃ phases of the IONPs have also been reported [46,48]. The data of the refinement process such as lattice parameters (a & c), unit cell volume (v), angle α , β , γ , full-width-half maxima parameters (viz. U, V, W), R_{wp} , R_{exp} , and χ^2 are summarized in Table 1. Satisfactory results of $\chi^2 = 3.69$ were achieved, while the wellcorrelated parameters $R_{wp} > R_{exp}$, the positive and negative values of u, v, w, and output plots imply the acceptance of our refinement process. The detailed satisfactory parameters for the Rietveld refinements are well explained by Brian [49]. The crystallite size (D) of the IONPs was estimated by Scherrer's formula [50].

$$D = \frac{K\lambda}{\beta cos\theta}$$

where K is Scherrer constant (0.9), λ is the wavelength of the Cu $K\alpha$ radiation (1.5406 Å), θ is the diffraction angle, and β is the FWHM (full-width half at half maximum) of the corresponding peak. A value of D = 21.29 nm of the (104) peak was obtained. It is slightly smaller than the one for α -Fe₂O₃ previously reported by Tadic et al. [51], indicating that peak broadening which can be observed in the XRD peaks of the IONPs. The crystal size

Molecules **2023**, 28, 1914 6 of 13

calculated from the XRD is less than the nanoparticle size estimated from the TEM images, which is expected in a polycrystalline material.

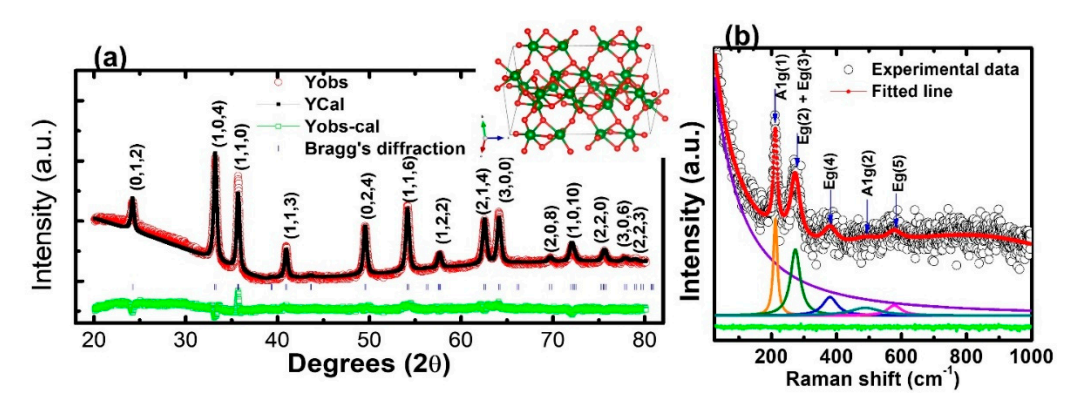


Figure 3. (a) Rietveld refinement of XRD spectra (inset: possible crystal structure of hexagonal IONPs). (b) Raman spectra of IONPs.

Table 1. Refinement structural parameters and agreement factors for IONPs at room temperature with space group R3C.

Parameters	a (Å)	c (Å)	U	V	W	R _{wp} (%)	R _{exp} (%)	x ²	$\alpha = \beta$	γ
Values	5.0302	13.7465	0.1806	-0.0475	0.1363	19.9	9.2	4.69	90	120

Figure 3b depicts the room temperature experimental Raman spectra (black hole) and fitted data (solid red line) for the IONPs. By analyzing the experimental data, using a Lorentzian function, five well-defined Raman modes were obtained in the wavenumber range 25–1000 cm $^{-1}$. The deconvolution peaks suggest that the dominant features of the Raman shift result from a hexagonal $\alpha\text{-Fe}_2\text{O}_3$. In the group theory to the point group of pure $\alpha\text{-Fe}_2\text{O}_3$, seven vibrational modes are expected to be Raman active: 2A1g + 5Eg [52]. We observed approximate peaks of 213 cm $^{-1}$ and 494 cm $^{-1}$ associated with the A1g phonon modes, and three other peaks (~273 cm $^{-1}$, 379 cm $^{-1}$, 580 cm $^{-1}$), which were related to the Eg phonon modes. The Raman active modes at room temperature for various forms of iron oxide are explained by Testa-Anta et al. [53]. These results corroborate the analysis of the X-ray diffraction peaks.

Magnetic properties of the sample were measured at a wide range of temperatures (10-390 K) at 1000 Oe, under field-cooled (FC) and zero-field-cooled (ZFC) conditions, as shown in Figure 4a. Both the ZFC and FC curves increase with a decrease in temperature, though the rate of change in the magnetization is greater in FC, while after a certain temperature, the magnetization starts decreasing. For ZFC, when the temperature decreases, the magnetization increases slowly and reaches its maximum, which corresponds to the blocking temperature (T_B), before decreasing sharply, which generates a large bifurcation at low temperatures. The magnetization of the FC curve achieves the maximum temperature of ~230 K, which is known as the saturation temperature (T_{sat}). After the T_{sat} , the spins gradually start freezing, showing spin glass-like behavior, which is attributed to the freezing of the disordered surface spins [26]. For both curves, we observed a decrease in magnetization below T_B, confirming the SPIONs nature. The bifurcation is a common feature in the FC and ZFC curves in the frustrated magnetic systems, such as spin glasses and cluster glasses [54,55]. The divergence between ZFC and FC started at a temperature far above T_B. This is due to the relatively broad size and shape distributions of the samples [56], which can be observed in the TEM micrographs. Further, the T_B values depend on the effective anisotropy and particle size, while T_B is the blocking temperature at which the thermal energy becomes compatible with the magnetic anisotropy energy barrier, where the particle goes in a superparamagnetic regime [57,58].

Molecules **2023**, 28, 1914 7 of 13

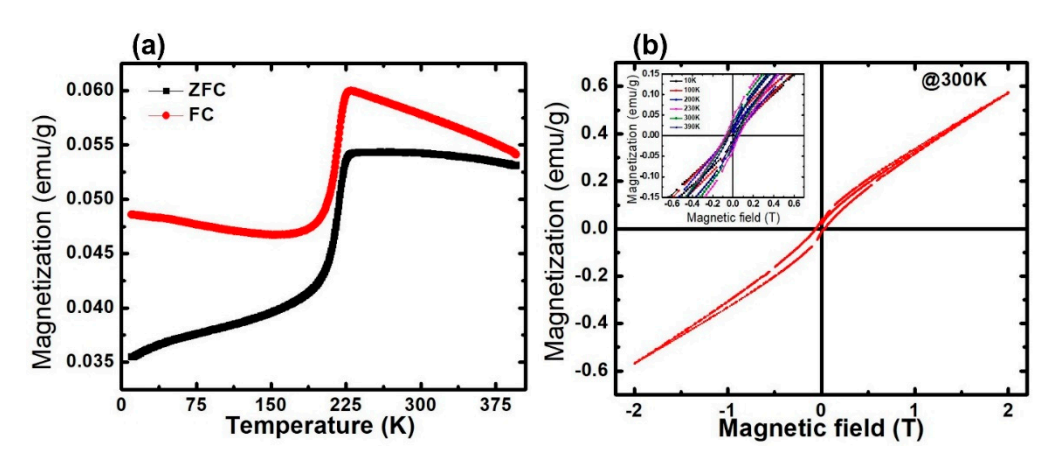


Figure 4. (a) Magnetization vs. temperature in FC and ZFC conditions recorded at 1000 Oe. (b) Magnetization vs. magnetic field hysteresis curve at 300 K (inset: magnetization vs. magnetic field at various temperatures (10–390 K) showing M_R and Hc).

The magnetic hysteresis M(H) of the IONPs, measured up to $\pm 2T$ at 300 K is shown in Figure 4b. The observed loop of M(H) indicates the superparamagnetic type of behavior that possesses a very low remnant and coercive field at the applied magnetic field (H). The Magnetic remnant polarization (M_R) and the coercive field (H_C) increase as the temperature increases, up to Tc, further increasing as the temperature starts to decrease. The sample shows a large M_R of approximately 0.0432 emu/g, with an H_C of approximately 0.0589T at 230 K. The observed values of M_R and H_C at various temperatures (10–390 K) is shown in the inset (Figure 5b) and summarized in Table 2.

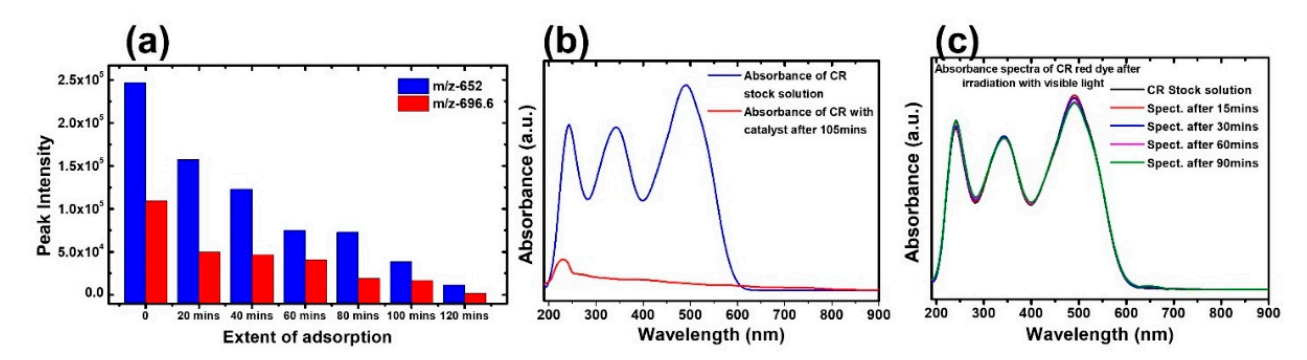


Figure 5. (a) Monitoring CR dye sodium salt and protonated structure in LC–MS. (b) Absorbance spectra of CR in the presence of IONPs. (c) Absorbance spectra in visible light in the absence of IONPs.

Table 2. M_R and H_C of the IONPs at various temperatures.

Temp. (K)	10	100	200	230	300	390
M _R (emu/g)	0.0196	0.0248	0.0338	0.0432	0.0357	0.0243
$H_C(T)$	0.0342	0.0247	0.0481	0.0589	0.0361	0.0208

IONPs are found to exhibit very strong adsorption of CR dye in the absence of light. Indeed, CR has a strong absorbance band at a wavelength of 486 nm. The absorbance intensity almost diminishes after 120 min (Figure 5b). The recent advances in the removal of dyes from wastewater and the possible adsorption mechanisms are explained in detail [59]. The stability of the CR solution in the absence of the catalyst was monitored both in the dark and following exposure to normal room light by measuring the absorbance every 15 min (Figure 5c). The absorbance remains unchanged, indicating that the dyes are very stable. To get more insight into the adsorption of the dyes of the Fe_2O_3 nanoparticles, a

Molecules **2023**, 28, 1914 8 of 13

time-dependent LC-tandem MS/MS-MS equipped with a triple quadrupole mass analyzer and electrospray ionization (ESI) interface was used. The spectrum obtained at each time step of the adsorption process shows a reduction in the intensity of the 696.6 m/z peak, with a corresponding decrease in the intensity at the 652.7 m/z peak for the same step. This reduction in intensity was consistent for both masses of the CR dye molecule. The CR was confirmed based on the two masses observed at 696.6 m/z and 652.7 m/z for the CR dye sodium salt and protonated structures, respectively (Figure 5a). The sodium ions are either separated during the chromatography process or exchanged for protons during the electrospray process by the mass spectrometer. The semi-quantitative study was performed based on the molecular ion (696.6 Da) and the fully protonated CR molecule (652.7 Da). The mass spectra obtained at various stages after the treatment with Fe₂O₃ nanoparticles are shown in Figure S3. As the treatment of the solution with the adsorbent progressed with sampling at intervals of 20 min, the intensity of the peak reduced and became almost undetectable. This shows the strong adsorption ability of the nanoparticles toward dyes. Our materials show superior/comparable efficiency compared with previously reported works [60-62].

Fe $_2$ O $_3$ nanoparticles are used to degrade organic pollutants in the presence of an oxidizing agent. In visible light, Fe $_2$ O $_3$ nanoparticles get easily excited and generate electrons and holes. The photogenerated electrons reduce Fe $_3$ + ions to Fe $_3$ + ions. The Fe $_3$ + H $_2$ O $_3$ ions oxidize CR through the Fenton mechanism [63]. The CR was monitored after the addition of H $_2$ O $_3$ in presence of visible light. The mass spectrum showed no peaks at m/z-696.6 and m/z-652.7, indicating complete degradation of the CR dye (Figure S4). The mass spectra of the CR stock solution and the sample solution treated with H $_2$ O $_3$ show vast differences in their chemical compositions, as shown in Figure S4a,b). Multiple peaks were obtained in the degradation reaction as compared to the adsorption reaction. Peaks at m/z ratios of 305.2, 327.0, 349.1, 365.0, 371.3, 393.1, 415.1, 429.2, 608.3, 652.3, and 696.3 were not observed in the spectrum in the presence of H $_2$ O $_2$ due to its complete degradation and the forming of other compounds of different masses to charge ratios. The catalytic degradation of CR and the subsequent degradation products have been well reported [64].

3. Experimental

3.1. Materials

Chemicals used in this experiment include urea (Sigma Aldrich, 99%) (St. Louis, MO, USA), block copolymer (Pluronic, F127; mol. wt. 12,500; Sigma Aldrich), iron nitrate hexahydrate (Fe(NO₃)₂·9H₂O; Sigma Aldrich, \geq 98%), hydrogen peroxide (H₂O₂; Alfa Aesar, 27% w/w) (Haverhill, MA, USA), Congo red (C.R.; Alfa Aesar, 99%), methanol, formic acid, and LC–MS grade water were purchased from Fisher Scientific (Fisher Scientific, Pittsburg, PA, USA).

3.2. Synthesis of IONPs

IONPs were synthesized using a polymer-controlled hydrothermal technique, and 0.30 g of the block copolymer was dissolved in 40 mL of deionized water using a magnetic stirrer (Wilmington, NC, USA). After the complete dissolution of the block copolymer, 1.25 g of Fe(NO₃)·9H₂O and 0.25 g of urea were added and stirred. The mixture was poured into an autoclave container (Dalian, China) and placed in a furnace at 90 °C for 12 h. The precipitation was centrifuged and washed four times using deionized water. Finally, the prepared sample was dried at 50 °C before calcination at 550 °C for 5 h at a ramping rate of 2 °C/min.

3.3. Characterization

Crystallinity and phase purity of IONPs were examined by X-ray diffraction (XRD) using a Rigaku Smart Lab X-ray Diffractometer (Rigaku Corporation, Japan), equipped with a Cu K α radiation source (λ = 1.5406 Å), operating at an accelerating potential of 40 kV, and a tube current of 44 mA. The X-ray spectra were recorded in the range of a

Molecules **2023**, 28, 1914 9 of 13

scattering angle $(2\theta) = 20$ to 80 degrees, at a slow scan rate of 0.01. The sensitive and non-destructive technique of Raman spectroscopy was used to investigate the changes in lattice vibrations and the phase purity of the IONPs. The room temperature Raman spectra of the powder sample were collected via a Horiba spectrometer T64000 (Kyoto, Japan) with Ar-ion laser excitation (514.5 nm) and attached to an optical microscope with $80 \times$ resolution. Scanning electron microscopy (SEM) (JEOL, Tokyo, Japan) and an energy dispersive X-ray (EDX) (JEOL, Tokyo, Japan), excited by an electron beam of energy 20 kV in a high-resolution of 40K, were used. The internal structure of nanoparticles was observed using a JEOL TEM 1210 electron microscope (JEOL, Tokyo, Japan) at an accelerating voltage of 120 kV. An X-ray photoelectron spectroscopy (XPS) (Thermofisher Scientific, Waltham, MA, USA), from Physical Electronics 5600ci with ultra-high vacuum ($\sim 6 \times 10^{-9}$ Torr), Al Kα source, analyzer diameter of 200 nm, and PHI Multipack 9.4, was used to study the chemical composition of the nanoparticles. The FTIR data were collected from the IRTracer-100, Shimadzu instrument in ATR mode (Kyoto, Japan). The field-dependent magnetic properties, M(H), and temperature-dependent magnetic measurements, M(T), of the IONPs, were recorded by the Quantum Design Dynacool fully automated, cryogen-free Physical Property Measurement System (PPMS) (Quantum Design, Inc., San Diego, CA, USA) within a temperature range from 10 K to 390 K, at a pressure $< 10^{-4}$ Torr, and at the magnetic field range from 0 T to 2 T. The hydrodynamic diameter and zeta potential were monitored using a Zetasizer Nano MS (Malvern-UK) at 25 °C and in an aqueous solution.

3.4. Adsorption Test

A 20 ppm solution of the CR dye was prepared for the experiment at room temperature, using deionized water as solvent. The adsorption ability of the nanoparticles was investigated using 20 mL of the 20 ppm solution with 10 mg adsorbent in an enclosed 100 mL glass reaction vessel. At specific time intervals, 5 mL of the sample solution was withdrawn and centrifuged before measuring the absorbance readings. The effect of light and oxidizing agents on the adsorption/degradation of dyes was also studied for comparison. A total of 20 mL of the 20 ppm CR dye was treated with 10 mg Fe₂O₃ nanoparticles, using 0.5 mL H₂O₂ in the presence of light, with continuous stirring. The absorbance of CR at 486 nm was monitored using an UV-Vis spectrophotometer (Pasco Scientific SE-3607) (Pasco, Roseville, CA, USA). The in-depth study of the adsorption/degradation of dyes was performed by utilizing a liquid chromatography–tandem mass spectrometry (LC-MS/MS) system equipped with a triple quadrupole mass analyzer and an electrospray ionization (ESI) interface (Agilent, Santa Clara, CA, USA). The optimized experimental conditions for chromatographic measurement are shown in Table S1.

4. Conclusions

Polycrystalline IONPs were successfully synthesized with a hydrothermal technique using a block copolymer and urea under desired synthesis conditions. The size distribution of nanoparticles observed in electron microscopy images proved that F127 works as an effective structure-directing agent, while a characteristic particle diameter of ~50 nm was examined through transmission electron microscopy. The EDX spectrum confirmed the presence of O and Fe elements and the orbital states Fe²⁺ and Fe³⁺ ions were analyzed via the XPS spectra. The Rietveld analysis of the X-ray diffractometer spectra showed the hexagonal phase symmetry dominant features of α -Fe₂O₃, which is further supported by the Raman analysis. The magnetic property measurement (both M_H and M_T) reveals the superparamagnetism on the IONPs with a maximum M_R and M_H of 0.0432 emu/g and 0.0589 T, respectively, at 230 K. The IONPs exhibited the very strong adsorption of the CR dye in the absence of light, the dye was almost diminished after 120 min. The systematic study of the adsorption of model dyes using LC-MS/MS triple quadrupole with electrospray ionization mass spectrometer showed a significant amount of dye was adsorbed on the nanoparticles and degraded in the presence of the oxidizing agent, H₂O₂. These properties of superparamagnetic behavior, with the strong ability to adsorb the

Molecules **2023**, 28, 1914 10 of 13

dye, lay the foundations for designing and synthesizing magnetic oxide nanoparticles for wastewater treatment and other catalytic applications.

Supplementary Materials: The following are available online at https://www.mdpi.com/article/10.3390/molecules28041914/s1, Table S1. Experimental parameters for LC-MS/MS measurement. Figure S1. Particle size distribution of nanoparticles from TEM images. Figure S2. SEM images of iron oxide nanoparticles synthesized in the absence of F127. Figure S3. The obtained mass spectra at various stages after the treatment with Fe₂O₃ nanoparticles. Figure S4. mass spectra of 20 ppm CR (a) before and (b) after treatment with IONPS and H_2O_2 .

Author Contributions: Conceptualization, M.K.B. and B.P.B.; methodology, M.K.B., M.D.A., K.S. and B.P.B.; validation, M.K.B., M.D.A. and K.S.; investigation, M.K.B., M.D.A., M.K.B. and M.D.A.; writing—original draft preparation, M.K.B., M.D.A., B.P.B. and S.D.; writing—review and editing, M.K.B., M.D.A., B.P.B., S.D., K.S., G.M. and R.S.K.; visu-alization, M.K.B. and B.P.B.; supervision, B.P.B., G.M. and R.S.K.; project administration, M.K.B.; funding acquisition, B.P.B., G.M. and R.S.K. All authors have read and agreed to the published version of the manuscript.

Funding: This work was financially supported by DoD (FA9550-20-1-0064) and PR NASA EPSCoR (80NSSC22M0025). BPB would like to thank the National Science Foundation; Research Initiation Award (2000310), Excellence in Research Award (2100710), PREM (2122067) USA, Joint School of Nanoscience and Nanoengineering, a member of the Southeastern Nanotechnology Infrastructure Corridor and National Nanotechnology Coordinated Infrastructure, which is supported by the National Science Foundation (Grant ECCS-1542174).

Institutional Review Board Statement: Not applicable.

Informed Consent Statement: Not applicable.

Data Availability Statement: The data that support the findings of this study are available from the corresponding author upon reasonable request.

Acknowledgments: Authors would like to thank the funding Agencies; NSF, DoD, and PR NASA EPSCoR. The authors acknowledge Rabin Dahal for SEM imaging, the valuable contributions of the Molecular Sciences Research Center (MSRC) Cupey, PR for XRD, SEM, EDS, XPS measurement, and Analytical Services Laboratory in the College of Agriculture and Environmental Sciences at the North Carolina A &T State University.

Conflicts of Interest: The authors have no conflict of interest.

Sample Availability: Samples are available from the authors.

References

- 1. Kang, S.; Shin, W.; Kang, K.; Choi, M.-H.; Kim, Y.-J.; Kim, Y.-K.; Min, D.-H.; Jang, H. Revisiting of Pd Nanoparticles in Cancer Treatment: All-Round Excellence of Porous Pd Nanoplates in Gene-Thermo Combinational Therapy. *ACS Appl. Mater. Interfaces* **2018**, *10*, 13819–13828. [CrossRef] [PubMed]
- Dinali, R.; Ebrahiminezhad, A.; Manley-Harris, M.; Ghasemi, Y.; Berenjian, A. Iron Oxide Nanoparticles in Modern Microbiology and Biotechnology. Crit. Rev. Microbiol. 2017, 43, 493–507. [CrossRef] [PubMed]
- 3. Paunovic, J.; Vucevic, D.; Radosavljevic, T.; Mandić-Rajčević, S.; Pantic, I. Iron-Based Nanoparticles and Their Potential Toxicity: Focus on Oxidative Stress and Apoptosis. *Chem. Biol. Interact.* **2020**, *316*, 108935. [CrossRef] [PubMed]
- 4. Janzen, C.; Knipping, J.; Rellinghaus, B.; Roth, P. Formation of Silica-Embedded Iron-Oxide Nanoparticles in Low-Pressure Flames. J. Nanopart. Res. 2003, 5, 589–596. [CrossRef]
- 5. Li, P.; Miser, D.E.; Rabiei, S.; Yadav, R.T.; Hajaligol, M.R. The Removal of Carbon Monoxide by Iron Oxide Nanoparticles. *Appl. Catal. B* **2003**, *43*, 151–162. [CrossRef]
- 6. Sharma, R.K.; Dutta, S.; Sharma, S.; Zboril, R.; Varma, R.S.; Gawande, M.B. Fe₃O₄ (Iron Oxide)-Supported Nanocatalysts: Synthesis, Characterization and Applications in Coupling Reactions. *Green Chem.* **2016**, *18*, 3184–3209. [CrossRef]
- 7. Slater, A.G.; Cooper, A.I. Function-Led Design of New Porous Materials. Science 2015, 348, aaa8075. [CrossRef]
- 8. Corot, C.; Robert, P.; Idée, J.M.; Port, M. Recent Advances in Iron Oxide Nanocrystal Technology for Medical Imaging. *Adv. Drug Deliv. Rev.* **2006**, *58*, 1471–1504. [CrossRef]
- 9. Mosayebi, J.; Kiyasatfar, M.; Laurent, S. Synthesis, Functionalization, and Design of Magnetic Nanoparticles for Theranostic Applications. *Adv. Heal. Mater.* **2017**, *6*, 1700306. [CrossRef]
- 10. Feng, L.; Cao, M.; Ma, X.; Zhu, Y.; Hu, C. Superparamagnetic High-Surface-Area Fe₃O₄ Nanoparticles as Adsorbents for Arsenic Removal. *J. Hazard. Mater.* **2012**, 217–218, 439–446. [CrossRef]

Molecules **2023**, 28, 1914 11 of 13

Jian, Y.; Yu, T.; Jiang, Z.; Yu, Y.; Douthwaite, M.; Liu, J.; Albilali, R.; He, C. In-Depth Understanding of the Morphology Effect of α-Fe₂O₃ on Catalytic Ethane Destruction. ACS Appl. Mater. Interfaces 2019, 11, 11369–11383. [CrossRef]

- 12. Ghosh, B.K.; Ghosh, N.N. Applications of Metal Nanoparticles as Catalysts in Cleaning Dyes Containing Industrial Effluents: A Review. *J. Nanosci. Nanotechnol.* **2018**, *18*, 3735–3758. [CrossRef]
- 13. Bhatia, P.; Nath, M. Green Synthesis of P-NiO/n-ZnO Nanocomposites: Excellent Adsorbent for Removal of Congo Red and Efficient Catalyst for Reduction of 4-Nitrophenol Present in Wastewater. *J. Water Process. Eng.* **2020**, *33*, 101017. [CrossRef]
- 14. Dhiman, P.; Sharma, G.; Alodhayb, A.N.; Kumar, A.; Rana, G.; Sithole, T.; ALOthman, Z.A. Constructing a Visible-Active CoFe₂O₄@Bi₂O₃/NiO Nanoheterojunction as Magnetically Recoverable Photocatalyst with Boosted Ofloxacin Degradation Efficiency. *Molecules* **2022**, 27, 8234. [CrossRef]
- 15. Wu, W.; Quanguo, A.E.; Ae, H.; Jiang, C. Magnetic Iron Oxide Nanoparticles: Synthesis and Surface Functionalization Strategies. *Nanoscale Res. Lett.* **2008**, *3*, 397. [CrossRef]
- 16. Liao, S.H.; Liu, C.H.; Bastakoti, B.P.; Suzuki, N.; Chang, Y.; Yamauchi, Y.; Lin, F.H.; Wu, K.C.W. Functionalized Magnetic Iron Oxide/Alginate Core-Shell Nanoparticles for Targeting Hyperthermia. *Int. J. Nanomed.* **2015**, *10*, 3315–3328. [CrossRef]
- 17. Mahmoudi, M.; Sahraian, M.A.; Shokrgozar, M.A.; Laurent, S. Superparamagnetic Iron Oxide Nanoparticles: Promises for Diagnosis and Treatment of Multiple Sclerosis. *ACS Chem. Neurosci.* **2011**, *2*, 118–140. [CrossRef]
- 18. Massironi, N.; Colombo, M.; Cosentino, C.; Fiandra, L.; Mauri, M.; Kayal, Y.; Testa, F.; Torri, G.; Urso, E.; Vismara, E.; et al. Heparin–Superparamagnetic Iron Oxide Nanoparticles for Theranostic Applications. *Molecules* **2022**, 27, 7116. [CrossRef]
- 19. Hurtado-Gallego, J.; Pulido-Reyes, G.; González-Pleiter, M.; Salas, G.; Leganés, F.; Rosal, R.; Fernández-Piñas, F. Toxicity of Superparamagnetic Iron Oxide Nanoparticles to the Microalga Chlamydomonas Reinhardtii. *Chemosphere* **2020**, 238, 124562. [CrossRef]
- Hirthna; Sendhilnathan, S. Enhancement in Dielectric and Magnetic Properties of Mg²⁺ Substituted Highly Porous Super Paramagnetic Nickel Ferrite Nanoparticles with Williamson-Hall Plots Mechanistic View. Ceram. Int. 2017, 43, 15447–15453.
 [CrossRef]
- 21. Tsuzuki, T.; McCormick, P.G. Mechanochemical Synthesis of Nanoparticles. J. Mater. Sci. 2004, 39, 5143–5146. [CrossRef]
- 22. Laurent, S.; Forge, D.; Port, M.; Roch, A.; Robic, C.; Vander Elst, L.; Muller, R.N. Erratum: Magnetic Iron Oxide Nanoparticles: Synthesis, Stabilization, Vectorization, Physicochemical Characterizations, and Biological Applications. *Chem. Rev.* **2010**, *110*, 2574. [CrossRef]
- 23. Moreno, E.M.; Zayat, M.; Morales, M.P.; Serna, C.J.; Roig, A.; Levy, D. Preparation of Narrow Size Distribution Superparamagnetic γ -Fe₂O₃ Nanoparticles in a Sol-Gel Transparent SiO₂ Matrix. *Langmuir* **2002**, *18*, 4972–4978. [CrossRef]
- 24. Xingu-Contreras, E.; García-Rosales, G.; García-Sosa, I.; Cabral-Prieto, A. Degradation of Methyl Orange Using Iron Nanoparticles with/without Support at Different Conditions. *Microporous Mesoporous Mater.* **2020**, 292, 109782. [CrossRef]
- 25. Tsang, S.C.; Caps, V.; Paraskevas, I.; Chadwick, D.; Thompsett, D. Magnetically Separable, Carbon-Supported Nanocatalysts for the Manufacture of Fine Chemicals. *Angew. Chem. Inter. Ed.* **2004**, *43*, 5645–5649. [CrossRef]
- 26. Thapa, B.; Diaz-Diestra, D.; Santiago-Medina, C.; Kumar, N.; Tu, K.; Beltran-Huarac, J.; Jadwisienczak, W.M.; Weiner, B.R.; Morell, G. T1- and T2-Weighted Magnetic Resonance Dual Contrast by Single Core Truncated Cubic Iron Oxide Nanoparticles with Abrupt Cellular Internalization and Immune Evasion. *ACS Appl. Bio. Mater.* **2018**, *1*, 79–89. [CrossRef]
- 27. Lin, C.R.; Chiang, R.K.; Wang, J.S.; Sung, T.W. Magnetic Properties of Monodisperse Iron Oxide Nanoparticles. *J. Appl. Phys.* **2006**, 99, 2004–2007. [CrossRef]
- 28. Kainz, Q.M.; Reiser, O. Polymer- and Dendrimer-Coated Magnetic Nanoparticles as Versatile Supports for Catalysts, Scavengers, and Reagents. *Acc Chem. Res.* **2014**, *47*, 667–677. [CrossRef]
- 29. Bentley, J.; Bastakoti, B.P. Block Copolymer Templated Synthesis of Mesoporous WO3/Carbon Nanocomposites. *J. Mater. Sci.* **2022**, *57*, 14772–14779. [CrossRef]
- 30. Olatidoye, O.; Thomas, D.; Bastakoti, B.P. Facile Synthesis of a Mesoporous TiO₂ film Templated by a Block Copolymer for Photocatalytic Applications. *N. J. Chem.* **2021**, *45*, 15761–15766. [CrossRef]
- 31. Bastakoti, B.P.; Sukegawa, H.; Wu, K.C.W.; Yamauchi, Y. Synthesis of Porous Iron Oxide Microspheres by a Double Hydrophilic Block Copolymer. *RSC Adv.* **2014**, *4*, 9986–9989. [CrossRef]
- 32. Darwish, M.S.A.; Mostafa, M.H.; Al-Harbi, L.M. Polymeric Nanocomposites for Environmental and Industrial Applications. *Int J. Mol. Sci.* **2022**, 23, 1023. [CrossRef]
- 33. Ozcan, O.; Ruhland, M.; Stahl, W. Shear Strength of Mineral Filter Cakes. In *Studies in Surface Science and Catalysis*; Elsevier Inc.: Amsterdam, The Netherlands, 2000; Volume 128, pp. 573–585.
- 34. Filippousi, M.; Angelakeris, M.; Katsikini, M.; Paloura, E.; Efthimiopoulos, I.; Wang, Y.; Zamboulis, D.; van Tendeloo, G. Surfactant Effects on the Structural and Magnetic Properties of Iron Oxide Nanoparticles. *J. Phys. Chem. C* 2014, 118, 16209–16217. [CrossRef]
- Bastakoti, B.P.; Huang, H.-S.; Chen, L.-C.; Wu, K.C.-W.; Yamauchi, Y. Block Copolymer Assisted Synthesis of Porous α-Ni(OH)₂
 Microflowers with High Surface Areas as Electrochemical Pseudocapacitor Materials. Chem. Commun. 2012, 48, 9150. [CrossRef]
- Li, Y.; Bastakoti, B.P.; Yamauchi, Y. Research Update: Triblock Copolymers as Templates to Synthesize Inorganic Nanoporous Materials. APL Mater. 2016, 4, 040703. [CrossRef]
- 37. Mills, P.; Sullivan, J.L. A Study of the Core Level Electrons in Iron and Its Three Oxides by Means of X-Ray Photoelectron Spectroscopy. *J. Phys. D Appl. Phys.* **1983**, *16*, 723–732. [CrossRef]

Molecules **2023**, 28, 1914 12 of 13

38. Jiang, L.; Wang, J.; Wu, X.; Zhang, G. A Stable Fe2O3/Expanded Perlite Composite Catalyst for Degradation of Rhodamine B in Heterogeneous Photo-Fenton System. *Water Air Soil Pollut*. **2017**, 228, 463. [CrossRef]

- 39. Muhler, M. The Nature of the Iron Oxide-Based Catalyst for Dehydrogenation of Ethylbenzene to Styrene 2. Surface Chemistry of the Active Phase. *J. Catal.* **1992**, *138*, 413–444. [CrossRef]
- 40. Yamashita, T.; Hayes, P. Analysis of XPS Spectra of Fe²⁺ and Fe³⁺ Ions in Oxide Materials. *Appl. Surf. Sci.* **2008**, 254, 2441–2449. [CrossRef]
- 41. Rajan, A.; Sharma, M.; Sahu, N.K. Assessing Magnetic and Inductive Thermal Properties of Various Surfactants Functionalised Fe₃O₄ Nanoparticles for Hyperthermia. *Sci. Rep.* **2020**, *10*, 15045. [CrossRef]
- 42. Saragi, T.; Santika, A.S.; Permana, B.; Syakir, N.; Kartawidjaja, M. Risdiana Synthesis and Properties of Iron Oxide Particles Prepared by Hydrothermal Method. *IOP Conf. Ser. Mater. Sci. Eng.* **2017**, *196*, 012025. [CrossRef]
- 43. Samrot, A.V.; Sahithya, C.S.; Selvarani, A.J.; Purayil, S.K.; Ponnaiah, P. A Review on Synthesis, Characterization and Potential Biological Applications of Superparamagnetic Iron Oxide Nanoparticles. *Curr. Res. Green Sustain. Chem.* **2021**, *4*, 100042. [CrossRef]
- 44. Finger, L.W.; Hazen, R.M. Crystal Structure and Isothermal Compression of Fe₂O₃, Cr₂O₃, and V₂O₃ to 50 Kbars. *J. Appl. Phys.* **2008**, *51*, 5362. [CrossRef]
- 45. Bhattarai, M.K.; Pavunny, S.P.; Katiyar, R.S. Effect of La and Sc Co-Doping on Dielectric and Ferroelectric Properties of PZT for Energy Storage Capacitors. *J. Appl. Phys.* **2021**, *130*, 34103. [CrossRef]
- 46. Krispin, M.; Ullrich, A.; Horn, S. Crystal Structure of Iron-Oxide Nanoparticles Synthesized from Ferritin. *J. Nanopart. Res.* **2012**, 14, 669. [CrossRef]
- 47. Teja, A.S.; Koh, P.Y. Synthesis, Properties, and Applications of Magnetic Iron Oxide Nanoparticles. *Prog. Cryst. Growth Charact. Mater.* **2009**, *55*, 22–45. [CrossRef]
- 48. Kuchma, E.; Kubrin, S.; Soldatov, A. The Local Atomic Structure of Colloidal Superparamagnetic Iron Oxide Nanoparticles for Theranostics in Oncology. *Biomedicines* **2018**, *6*, 78. [CrossRef]
- 49. Toby, B.H. R Factors in Rietveld Analysis: How Good Is Good Enough? Powder Diffr. 2006, 21, 67–70. [CrossRef]
- 50. Rabiei, M.; Palevicius, A.; Monshi, A.; Nasiri, S.; Vilkauskas, A.; Janusas, G. Comparing Methods for Calculating Nano Crystal Size of Natural Hydroxyapatite Using X-Ray Diffraction. *Nanomaterials* **2020**, *10*, 1627. [CrossRef]
- 51. Tadic, M.; Trpkov, D.; Kopanja, L.; Vojnovic, S.; Panjan, M. Hydrothermal Synthesis of Hematite (α-Fe₂O₃) Nanoparticle Forms: Synthesis Conditions, Structure, Particle Shape Analysis, Cytotoxicity and Magnetic Properties. *J. Alloys Compd.* **2019**, 792, 599–609. [CrossRef]
- 52. Testa-Anta, M.; Ramos-Docampo, M.A.; Comesaña-Hermo, M.; Rivas-Murias, B.; Salgueiriño, V. Raman Spectroscopy to Unravel the Magnetic Properties of Iron Oxide Nanocrystals for Bio-Related Applications. *Nanoscale Adv.* 2019, 1, 2086–2103. [CrossRef] [PubMed]
- 53. Lassoued, A.; Dkhil, B.; Gadri, A.; Ammar, S. Control of the Shape and Size of Iron Oxide (α-Fe₂O₃) Nanoparticles Synthesized through the Chemical Precipitation Method. *Results Phys.* **2017**, *7*, 3007–3015. [CrossRef]
- 54. Kundu, A.K.; Nordblad, P.; Rao, C.N.R. Nonequilibrium Magnetic Properties of Single-Crystalline La_{0.7}Ca_{0.3}CoO₃. *Phys. Rev. B Condens. Matter Mater. Phys.* **2005**, 72, 144423. [CrossRef]
- 55. Dugu, S.; Bhattarai, M.K.; Kumari, S.; Instan, A.A.; Pradhan, D.K.; Holcomb, M.; Scott, J.F.; Katiyar, R.S. Observation of Relaxor-Ferroelectric Behavior in Gallium Ferrite Thin Films. *Appl. Surf. Sci.* **2020**, 523, 146459. [CrossRef]
- 56. Hu, H.; Yuan, Y.; Lim, S.; Wang, C.H. Phase Structure Dependence of Magnetic Behaviour in Iron Oxide Nanorods. *Mater. Des.* **2020**, *185*, 108241. [CrossRef]
- 57. Guardia, P.; Batlle-Brugal, B.; Roca, A.G.; Iglesias, O.; Morales, M.P.; Serna, C.J.; Labarta, A.; Batlle, X. Surfactant Effects in Magnetite Nanoparticles of Controlled Size. *J. Magn. Magn. Mater.* **2007**, *316*, e756–e759. [CrossRef]
- 58. Issa, B.; Obaidat, I.M.; Albiss, B.A.; Haik, Y. Magnetic Nanoparticles: Surface Effects and Properties Related to Biomedicine Applications. *Int. J. Mol. Sci.* **2013**, *14*, 21266–21305. [CrossRef]
- 59. Dutta, S.; Gupta, B.; Srivastava, S.K.; Gupta, A.K. Recent Advances on the Removal of Dyes from Wastewater Using Various Adsorbents: A Critical Review. *Mater. Adv.* **2021**, 2, 4497–4531. [CrossRef]
- 60. Lei, C.; Zhu, X.; Le, Y.; Zhu, B.; Yu, J.; Ho, W. Hierarchically Porous NiO–Al₂O₃ Nanocomposite with Enhanced Congo Red Adsorption in Water. *RSC Adv.* **2016**, *6*, 10272–10279. [CrossRef]
- 61. Peydayesh, M.; Rahbar-Kelishami, A. Adsorption of Methylene Blue onto Platanus Orientalis Leaf Powder: Kinetic, Equilibrium and Thermodynamic Studies. *J. Indus. Eng. Chem.* **2015**, *21*, 1014–1019. [CrossRef]
- 62. Ayad, M.; Salahuddin, N.; Fayed, A.; Bastakoti, B.P.; Suzuki, N.; Yamauchi, Y. Chemical Design of a Smart Chitosan–Polypyrrole–Magnetite Nanocomposite toward Efficient Water Treatment. *Phys. Chem. Chem. Phys.* **2014**, *16*, 21812–21819. [CrossRef]

Molecules **2023**, 28, 1914 13 of 13

63. Tsuneda, T. Fenton Reaction Mechanism Generating No OH Radicals in Nafion Membrane Decomposition. *Sci. Rep.* **2020**, *10*, 18144. [CrossRef]

64. Erdemoğlu, S.; Aksu, S.K.; Sayilkan, F.; Izgi, B.; Asiltürk, M.; Sayilkan, H.; Frimmel, F.; Güçer, Ş. Photocatalytic Degradation of Congo Red by Hydrothermally Synthesized Nanocrystalline TiO₂ and Identification of Degradation Products by LC-MS. *J. Hazard. Mater.* **2008**, 155, 469–476. [CrossRef]

Disclaimer/Publisher's Note: The statements, opinions and data contained in all publications are solely those of the individual author(s) and contributor(s) and not of MDPI and/or the editor(s). MDPI and/or the editor(s) disclaim responsibility for any injury to people or property resulting from any ideas, methods, instructions or products referred to in the content.